Simulations of indentation-induced phase transformations in crystalline and amorphous silicon

V. I. Ivashchenko,[1] P. E. A. Turchi,[2] and V. I. Shevchenko[1]
[1]*Institute of Problems of Materials Science, National Aacademy of Sciences of Ukraine, 3 Krzhyzhanovsky Street, 03142 Kyiv, Ukraine*
[2]*Lawrence Livermore National Laboratory (L-352), P. O. Box 808, Livermore, CA 94551, USA*
(Received 27 June 2007; revised manuscript received 20 February 2008; published 11 July 2008)

The pressure- and indentation-induced phase transformations in crystalline (*cd*) and amorphous (*a*) silicon are studied by using molecular dynamics simulations based on the modified Tersoff potential. The $sp^3s^\star$ tight-binding scheme is employed to gain insight into the origin of the change in conductivity during nanoindentation. The Gibbs free energy calculations predict the following pressure-induced phase transitions: *cd*-Si $\rightarrow \beta$-tin Si(β-Si) (11.4 GPa); *cd*-Si $\rightarrow$ high density amorphous phase (HDA) (22.5 GPa); *a*-Si $\rightarrow \beta$-Si (2.5 GPa); *a*-Si $\rightarrow$ HDA (8.4 GPa). Simulations of nanoindentation of crystalline silicon reveal discontinuities in the load-displacement curves. In the loading curves of the *cd*-Si (100) substrate, the pop-in is assigned to the appearance of the β-tin Si phase. During unloading, the pop-out is due to the formation of a low-density amorphous phase *a*-Si. The *a*-Si $\rightarrow$ HDA transformation takes place during nanoindentation of *a*-Si in loading regime. Upon unloading the *a*-Si phase is preserved. The structural transformations in *cd*-Si and *a*-Si during nanoindentation are treated in terms of triaxial and uniaxial compressions of the respective bulk samples. A change in conductivity from semiconducting to metallic during nanoindentation of the *cd*-Si (100) and *a*-Si slabs is explained in terms of a transformation of the localized electronic states in the band gap region. The results are compared to those of available theoretical models and experiments.

DOI: 10.1103/PhysRevB.78.035205 PACS number(s): 61.43.Dq, 71.15.Pd, 71.23.Cq

I. INTRODUCTION

It is well known that nanoindentation is a powerful probe to estimate the strength properties of thin films and in particular, nanohardness and elastic modulus.[1–3] When interpreting nanoindentation results, it is important to have a precise knowledge of the structural transformations (ST) that may occur during nanoindentation. The state of the art in the study of ST in diamondlike crystalline silicon (*cd*-Si) caused by indentation has been thoroughly described in Ref. 3. Since different high-pressure phases of silicon are observed in the indent region,[3] it is useful to consider the ST that occur in silicon under hydrostatic pressure. Bulk silicon *cd*-Si (diamondlike phase, with space group $Fd3m$) undergoes the following phase transformations under compression and upon decompression: The *cd*−Si structure transforms to the tetragonal body-centered metallic β-tin (β-Si) phase ($I4_1/\mathrm{amd}$) at $\sim$11–12.5 GPa.[4,5] The β-Si phase undergoes a transformation to the related *Imma* structure at 13 Gpa.[6,7] A further increase in pressure leads to the appearance of a primitive hexagonal *hd* ($P6_3/\mathrm{mmc}$) structure near 16 Gpa.[5–8] It is worth noting that bulk Si does not transform back to the ground-state *cd*-Si structure upon full pressure release. Instead, a variety of metastable crystalline and amorphous phases are observed.[9,10] Among them, the cubic body-centered *bc*8 ($Ia3^-$), tetragonal *st*12 ($P4_222$), and rhombohedral *r*8 ($R3^-$) structures have been identified.[9,11,12] Amorphous semiconductor silicon (*a*-Si) transforms to the metallic high-density amorphous phase (HDA) at approximately 10 GPa.[13]

In the present investigation we deal with indentation caused by a truncated hemispherical diamond indenter; therefore, to a first-order approximation we will focus on an analysis of the results of indentation by assuming the tip to be spherical.[14–16] The experimental studies of the indent during different stages of indentation carried out by using electrical resistivity measurements, x-ray diffraction, Raman spectroscopy, and optical spectroscopy[3] clearly show the existence during indentation of a dense semiconductor-to-ductile metal phase transformation (*cd*-Si $\rightarrow \beta$-Si). Upon unloading, a tetragonal body-centered to amorphous semiconductor phase transformation is observed.[17] However, an increase in indentation load leads to the appearance of some crystalline β-Si and *cd*-Si spots in the transferred amorphous zone after complete unloading.[18,19] The load-displacement curves show common features related to the so called "pop-in" and "pop-out" events, where the indenter suddenly enters deeper into the material without any additional force being applied.[14–16,20] The origin of the pop-ins and pop-outs in *cd*-Si under nanoindentation is often assigned to phase transitions, although other explanations were also suggested. In particular, a dislocation-based explanation has been suggested.[3] Both pressure and resistance changes imply that the *cd*-Si $\rightarrow \beta$-Si transformation occurring during indentation is similar to that observed in high-pressure experiments.[4,5]

As for amorphous silicon, indentation experiments on *a*-Si prepared by homogeneous chemical vapor deposition also indicated transformation to an electrically conducting phase with the remaining phase after unloading being a low density *a*-Si.[21] So, the initial *a*-Si structure transforms to the metallic HDA phase upon loading and to a low density *a*-Si again during unloading, which is consistent with the results on pressure-induced semiconductor-to-metal transition in amorphous silicon reported by Shimomura *et al.*[13] However, other indentation work on ion-implanted *a*-Si [22] is not consistent with these findings. In particular, it has been shown that both the relaxed and unrelaxed states undergo a phase transformation to a metallic phase upon loading and can undergo further phase transformations to the polycrystalline phases *bc*8 and *r*8 during unloading, whereas no evidence of

phase transformations was found in the unrelaxed state of *a*-Si under low-load indentation.

Phase transformations in silicon under pressure were theoretically investigated with a pseudopotential approach (PPA),[23] molecular dynamics (MD) based on the Car–Parrinello formalism,[24] the tight-binding (TB) model,[25,26] and empirical interatomic potentials.[3,27–30] In particular, using PPA, Zandiehnadem and Ching[23] successfully reproduced most crystalline phases of Si that occur under pressure. However Car–Parrinello MD simulations of a compression of *cd*-Si did not reveal the β-Si phase, but instead a *hd* structure was detected at 30 Gpa.[24] Durandurdu and Drabold[25,26] successfully accounted for the high-pressure phases of amorphous silicon by using a tight-binding molecular dynamics (TB-MD) scheme. Their theoretical predictions of the transformations among the *cd*-Si, β-Si, and *a*-Si phases under pressure are consistent with the experimental findings.

The indentation-induced ST in *cd*-Si were analyzed in the framework of MD simulations based on an empirical potential that combines the Tersoff (Si-Si and C-C interactions) and the Morse (Si-C interactions) potentials.[3,27–30] The theoretical investigations of the structural transformations during indentation of the Si (100) slab revealed the following path: *cd*-Si $\rightarrow$ β-Si and β-Si $\rightarrow$ *a*-Si during loading and unloading, respectively. As for other related materials, MD simulations of nanoindentation with a rigid square-base indenter of crystalline (3*C*-SiC), nanocrystalline (*nc*-SiC), amorphous (*a*-SiC) silicon carbides,[31–33] and crystalline GaAs[34] should be mentioned. Since the modeling[31–33] was based on an empirical potential determined from various modifications of crystalline silicon carbide, only chemically ordered structures were revealed during loading. The calculated load-displacement curves of 3*C*-SiC and *a*-SiC exhibit a series of load drops caused by plastic deformation. In the case of *nc*-SiC, the simulations predict a crossover from intergranular continuous deformation to intragranular discrete deformation at a critical indentation depth. For GaAs the pop-in event observed during nanoindentation is explained by a phase transformation from a zincblende to a rocksaltlike structure.[34]

From this short review it follows that theoretical studies of ST in amorphous silicon occurring during indentation are still lacking, and theoretical investigations of nanoindentation of *cd*-Si are in an infant stage. As was mentioned above, during a nanoindentation of *cd*-Si, the conductivity of the indented region changes from semiconducting to metallic; however, a possible mechanism for such a change is still lacking. Hence, it is of interest to perform MD simulations for this class of materials to investigate new possible mechanisms of structural transformations and electronic transport properties during nanoindentation, and to add new details to the available theoretical models.

The present investigation contains the theoretical results on nanoindentation of crystalline and amorphous silicon obtained with MD simulations based on the modified Tersoff potential. In the case of the nanoindentation of *cd*-Si, the (100) orientation of the substrate surface facing the nanoindenter is considered. To interpret the nanoindentation results, we first investigate the pressure-induced phase transitions in *cd*-, *nc*-, and *a*-Si. The electronic structure changes of the aggregate beneath the indenter are studied on the basis of an analysis of the electronic localization in the band-gap region. The results are then discussed and compared to the available experimental and theoretical data.

The paper is organized as follows. In Sec. II, the computational procedures that include the MD simulations based on the Tersoff potential, the scheme for studying nanoindentation, and the $sp^3s^\star$ tight-binding scheme are presented. Secs. III and IV contain the results and discussion. The theoretical findings on crystalline and noncrystalline silicon phases are presented in separate subsections. The mechanisms that lead to the semiconductor-to-metal transitions during nanoindentation are also discussed. Finally, generalization and conclusions are presented in Sec. V.

II. SIMULATION SETUP

The structural transformations that occur in silicon will be investigated in the following sections with MD simulations based on the Tersoff potential.[35] Because this potential has been fitted to the corresponding equilibrium properties, its predictive capability in the case of significant strains should be revisited. To validate the applicability of the potential to the present study, nonrelativistic band structure calculations for *cd*-Si within density functional theory were carried out using the full-potential linearized-augmented plane-wave (FLAPW) method.[36] The semicore states were considered as valence states, while the core states were treated as atomic-like states. The wave functions were expanded in a set of augmented plane waves with wave vectors up to $kR=8.0$, where R is the radius of the muffin-tin spheres. Inside these spheres, the potential and the charge density were expanded in spherical harmonics up to $l=8$. The criterion of convergence for the total energy was 0.1 mRy/f.u. The generalized gradient approximation (GGA)[37] and the local density approximation (LDA)[38] for the exchange-correlation potential were employed. For the k integration, the modified tetrahedron method was used throughout.[36] For the tetragonal and cubic structures, we took a (8 8 8) Monkhorst–Pack k-point sampling in the Brillouin zone. The FLAPW structural characteristics, together with the data of other authors, are presented in Table I. In Fig. 1, we compare the reduced total energies (the minima of the total energy curves for *cd*-Si were superposed with the cohesive energy predicted by the Tersoff potential for this material) of *cd*-Si and β-Si as functions of volume as determined from FLAPW calculations, MD simulations based on the Tersoff potential, and orthogonalized linear combination of atomic orbitals (OLCAO) calculations.[23] One can see that there is no preferred method that would accurately reproduce the structural characteristics. Nevertheless, we note that both the Tersoff potential and the generalized gradient approximation full-potential linearized-augmented plane-wave (GGA FLAPW) method give acceptable results, whereas the OLCAO approach overestimates the transition pressure. The main conclusion that can be drawn from this comparison is that the Tersoff potential provides quite acceptable structural characteristics for the *cd*-Si and β-Si phases as functions of pressure. Since our study focuses

TABLE I. Results from the FLAPW method and from calculations based on the empirical Tersoff potential (EP) for *cd*-Si and β-Si: lattice constant (a and c/a), cell volume (V), bulk moduli (B), pressure derivative of B (B'), total energy (E_T), transition volume of the *cd*-Si-β-Si transition determined from the E-V curves (cf. Fig. 1) in units of V (*cd*-Si), and transition pressure (P_0). The FLAPW calculations were carried out within the LDA and GGA for the exchange-correlation potential. The results from the pseudopotential approach (PPA)[39] and the self-consistent orthogonalized linear combination of atomic orbitals method (OLCAO)[23] are also presented. For the sake of comparison, the experimental data (EXP) that were summarized in Refs. 4, 5, 23, and 39 are also reported.

Method	Phase	a (Å)	c/a	V (Å^3/at.)	B (Gpa)	B'	E_T (eV/at.)	$V/V(cd)$	P_0 (GPa)
LDA	*cd*-Si	5.406	1.000	19.75	97.0	4.2	0.000	0.94	6.4
	β-Si	4.722	0.556	14.64	117.3	4.3	0.204	0.72	
GGA	*cd*-Si	5.475	1.000	20.51	89.7	4.1	0.000	0.91	8.5
	β-Si	4.778	0.566	15.16	109.4	4.1	0.283	0.70	
EP	*cd*-Si	5.432	1.000	20.03	97.5	4.4	0.000	0.91	11.4
	β-Si	4.902	0.524	15.43	137.5	4.6	0.327	0.72	
PPA	*cd*-Si	5.451	1.000	20.25	98.0	3.2	0.000		8.9
	β-Si	4.822	0.552	15.47	119.0		0.266		
OLCAO	*cd*-Si	5.430	1.000	20.01	105.0	4.2	0.000	0.89	15.4
	β-Si	4.883	0.552	16.07			0.385	0.71	
EXP	*cd*-Si	5.429	1.000	20.00	99.0	4.2	0.000	0.91–0.92	11.3–12.5
	β-Si	4.686	0.552	14.00				0.71	

on the structural changes that occur in Si under compressive strain, the Tersoff potential is therefore considered adequate.

By using MD simulations based on the Tersoff potential[35] in the Andersen constant number of particles–pressure–temperature (NPT) ensemble with periodic boundary conditions (PBC), we generated three groups of samples. The first group includes the cubic 512-atom *cd*-Si, *a*-Si, β-Si, and HDA structures that will be used to calculate the Gibbs free energy and determine the electronic structure. The *a*-Si and HDA structures were generated according to the procedure described in Ref. 40. The transition pressure between two silicon phases at zero temperature was calculated from well-known thermodynamics and from the computed P-V diagrams. For this purpose, all of the final silicon samples, generated with PBC, were equilibrated at 10 K, and then the atomic configurations were relaxed by setting all of the particle velocities to zero when the potential energy had a tendency to rise after each time step. In the second group, the cubic 4096-atom samples of *cd*-Si and *a*-Si were generated. The large-scale structures are needed for MD simulations of uniform and uniaxial compressions. Simulations were carried out at 500 K in the NPT ensemble with PBC that maintain a constant bulk modulus. Finally, the third group includes the 9216-atom samples ($12\times12\times8$ in units of a_0=5.43 Å) of *cd*-Si and *a*-Si that were used to carry out the nanoindentation tests. Let us briefly describe the procedure that was considered to generate the samples of the second and third groups. The diamondlike *cd*-Si samples were obtained after 20 ps equilibration time of the corresponding crystals at 300 K. The amorphous structures were generated as follows. The diamondlike initial structures were heated up to 4000 K, equilibrated during 20 ps at this temperature and then cooled down to 300 K with a cooling rate of about 10^{13} K/s. The final samples were equilibrated at 300 K for 20 ps. The 9216-atom structures were equilibrated after removal of the PBC.

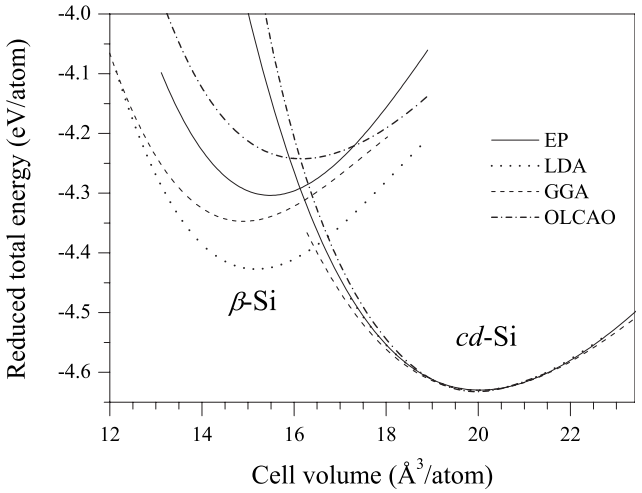

FIG. 1. Reduced total energies (E_T) of *cd*-Si and β-Si as functions of cell volume calculated by using the empirical Tersoff potential (EP) and the FLAPW method within the LDA and GGA. For comparison, the OLCAO results[23] are also shown.

To perform a nanoindentation on the generated slabs, we used the following approach. At first the diamond indenter was generated with a hemispherical (976 atoms) or truncated hemispherical (962 atoms) shape. The motivation of the latter choice came about since, in practice, a real spherical indenter is blunt, and its shape significantly deviates from ideality. The large diameter of the blunt indenter was 27.1 Å, with a height of 11.6 Å. The atoms located on the top surface of the indenter and on the outer surfaces of the silicon substrates were thermostatted to maintain a temperature of 300 K. The boundary atoms of the silicon substrate were fixed except those located on the upper surface that were considered as "Newtonian atoms." This protocol was also

adopted in a number of other theoretical studies.[27–30] The distance between the lowest plane of the diamond indenter and the upper surface of the silicon samples averages 2.4 Å. Nanoindentation occurs as follows: (1) a discrete displacement of the indenter toward the sample surface by 0.005 Å is applied; (2) the atoms on the top indenter surface are being fixed; (3) the system is then equilibrated according to the loading rate; (4) the constraint on the fixed position of the atoms belonging to the top plane of the indenter is relaxed, and the average force F_{zz} acting on the indenter atoms along the z direction (i.e., the normal to the Si slab) is calculated. The same procedure was used during unloading, i.e., when the indenter is moved up away from the sample. The rates of loading were 5, 50, and 250 m/s, whereas the rates of unloading were 5, 25, and 250 m/s. The chosen indentation conditions provide a maximum hydrostatic pressure under the indenter of approximately 11 GPa.

In experiments, at any loading rate and after complete unloading, a clear indent forms. In the simulations, because of the attraction between Si and C atoms, the silicon atoms will move together with the indenter, thereby, influencing the indent shape and the ST that take place beneath the indenter. Therefore, we knowingly reduced the mixing parameter χ_{SiC} (Ref. 35) from 1.0086 to 0.6 to guarantee the predominance of repulsive Si-C interactions. So our approach was close to the indentation procedure discussed in Refs. 31–33 for which the 3C-SiC indenter was held rigid, and only the steric repulsion was considered between indenter atoms and the substrate. Additional details will be provided later. Here we note that the overestimation of the repulsion between substrate and indenter atoms will lead to an enhancement of the forces exerted on the indenter by the substrate. However such an approach is quite justified since it allows us to investigate indentation-induced ST during loading and unloading with the same level of accuracy.

The semiconductor-to-metal transitions were determined by means of a comparative analysis of the localization of the electronic states for the different phases. For this purpose, the mean-square charges $Q2$ were calculated for each eigenvalue of the $sp^3s^\star$ TB matrix, according to the procedure reported in Refs. 25 and 26. In brief, the charge $q(n,E)$ associated with each eigenvalue with energy E and an atomic site n is calculated. Since the quantity $q(n,E)$ summed over all atoms should equal unity, it is not suitable for determining the degree of localization of the electronic states. Instead, a mean-square charge $Q2$ is introduced[25,26]

$$Q2(E) = N\sum_n q(n,E)^2, \tag{1}$$

where N is the number of atoms in the sample. From the analysis of $Q2$, one can evaluate the localization of a specific state for comparison purposes.

The details of the computations with the orthogonal $sp^3s^\star$ TB scheme were described elsewhere.[40] In previous studies[40–42] it was shown that the set of TB two-center parameters that were used in the TB-MD simulations provided reasonable atomic and electronic structures for silicon-based amorphous alloys. In this work, the eigenvalues were calculated at the Γ point of the Brillouin zone, which is reasonable for a cubic cell with 512 atoms. The density of state (DOS) of cd-Si obtained from our TB scheme shows a semiconducting band gap in the range (0.0, 1.16) eV.

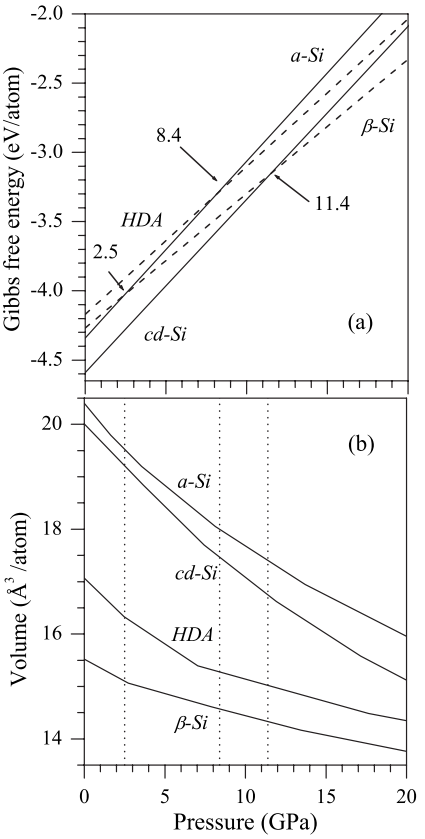

FIG. 2. Calculated Gibbs free energy (a) and volume per atom (b) for the diamondlike (cd), β-Sn (β), amorphous (a), high-density amorphous (HDA), and nanocrystalline (nc) phases of silicon as functions of pressure. The numbers in (a) and the vertical dotted line in (b) refer to the transition pressures.

III. PRESSURE-INDUCED PHASE TRANSFORMATIONS

The relative stability of the phases of silicon as a function of pressure can be estimated by a comparison of their Gibbs free energies $G=E_{Coh}+PV$ at zero temperature. The point where the Gibbs energy curves cross determines the transition pressure (P_0) of a pressure-induced phase transition between the two phases. In Fig. 2, the calculated Gibbs free energies and volumes of the silicon phases are plotted as functions of pressure. The transition pressures and transition volumes of the silicon phases are summarized in Table II. First of all we note that the characteristics of pressure-induced ST that are deduced from the Gibbs free energy calculations are very close to those obtained with the TB method,[25,26] and to the corresponding experimental results. However, the Tersoff potential-based calculations overestimate the volume reduction with increasing pressure as compared to the TB results. The calculated Gibbs free energy curves confirm the conclusion of Durandurdu and Drabold on the impossibility of a phase transition between β-Si and the HDA phase.[26] We obtained a slightly lower value P_0 for

TABLE II. Transition pressure P_0 and volumes $V_1(P_0)$ and $V_2(P_0)$ between different silicon phases at P_0. The calculated equilibrium volume per atom of *cd*-Si is V_{cd}=20.03 Å^3/atom. In these units the equilibrium volumes of *cd*-Si, *β*-Si, *a*-Si, and HDA at zero pressure are 1.00, 0.77, 1.02, and 0.85, respectively.

Phase transition	P_0 (Gpa)	$V_1(P_0)-V_2(P_0)$ (In units of V_{cd})
cd-Si→*β*-Si	11.4[a], 9[b], 15.4[c], 11.3–12.5[d], 11[e]	0.91–0.72[a], 0.92–0.68[b], 0.89–0.71[c], 0.91–0.71[g]
cd-Si→HDA	22.5[a], 15.0[b]	0.74–0.71[a], 0.89–0.65[b]
a-Si→*β*-Si	2.5[a], 2.5[b]	0.98–0.75[a], 0.98–0.72[b]
a-Si→HDA	8.4[a], 9.0[b], 10[f]	0.90–0.77[a], 0.92–0.69[b]

[a]Present investigation.
[b]TB investigation (Ref. 26).
[c]LCAO calculations (Ref. 23).
[d]Experimental investigations (Ref. 5).
[e]Experimental investigations (Ref. 4).
[f]Experimental investigations (Ref. 13).
[g]Experimental investigations (Refs. 5 and 8).

the *a*-Si→HDA transition than in our earlier work,[40] and this can be attributed to an improved structure of *a*-Si and to a slightly more appropriate relaxation procedure used in the present investigation.

The results presented in Fig. 1 allow us to predict the pressure of transformation between the *cd*-Si and *β*-Si phases. This ST could be observed dynamically from our constant-pressure MD simulations. As mentioned above, we performed triaxial and uniaxial compressions and decompressions of the 4096-atom *cd*-Si and *a*-Si samples at 500 K. This temperature was chosen to reflect the conditions under which nanoindentation tests are usually done. In Fig. 3 we show the structural and energetic characteristics of the samples as functions of pressure. The pair-correlation function and bond-angle distribution for *cd*-Si are presented in Fig. 4. For comparison these characteristics are also shown for the HDA phase. For both samples, in the volume-pressure curves, a potential barrier is observed, with a higher value for the crystalline than the amorphous sample. The drastic reduction in volume indicates a first-order phase transition. The transition pressures are approximately 22 and 9 GPa for *cd*-Si and *a*-Si, respectively, that are close to the corresponding values of 22.5 and 8.4 GPa predicted from thermodynamics (cf. Fig. 2). An analysis of the pair correlation function (PCF) and bond-angle distributions shows that the HDA phases form just below the transition pressures. The formation of a HDA phase in *a*-Si under uniform pressure was also reported in Refs. 25, 26, and 40. In Fig. 3 the 4096-atom HDA structure is not shown since it will be discussed in detail below. Upon decompression, these HDA phases are preserved. Uniaxial compression of *cd*-Si gives rise to a new phase at approximately 11.5 GPa that is identified as the *β*-Si structure. This phase is stable upon complete decompression. To the best of our knowledge, there are no MD predictions of the *cd*-Si to *β*-Si transition under hydrostatic pressure. Given these findings we conclude that in real crystals, such a transition can preferentially occur in regions of tetragonal strain.

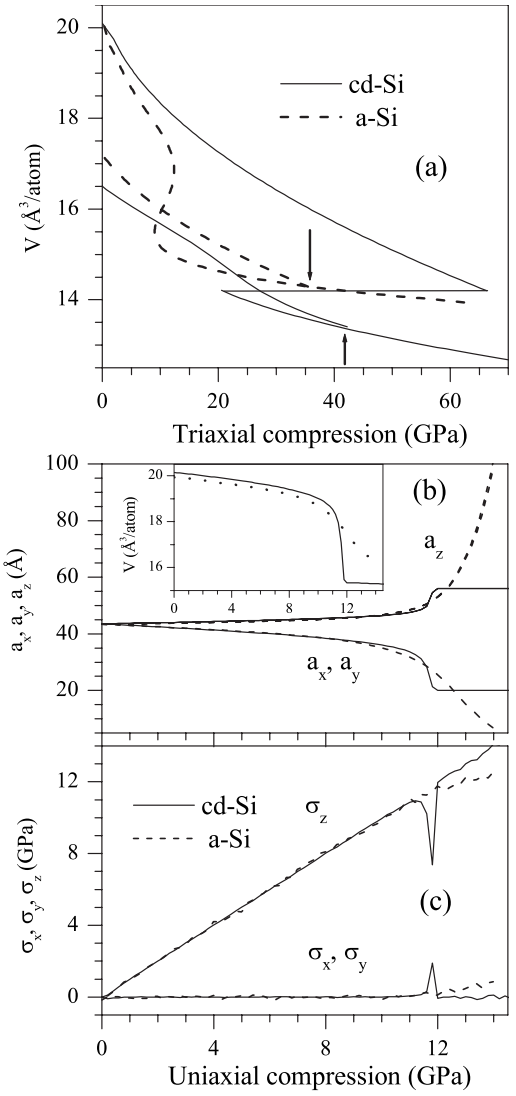

FIG. 3. Change in cell volume (V) for *cd*-Si and *a*-Si under triaxial compression and decompression (a). Change of lattice parameters (a_x, a_y, a_z), stresses $(\sigma_x, \sigma_y, \sigma_z)$, and cell volume (in the inset) for *cd*-Si and *a*-Si under uniaxial compressions (b, c). Arrows in (a) indicate the onsets of decompression.

Uniaxial compression of *a*-Si occurs slowly without a drastic decrease in volume. The sample flattens, and its thickness decreases to 5–6 Å at P=12–14 GPa. Above this pressure the sample fails.

IV. INDENTATION-INDUCED PHASE TRANSFORMATIONS

A. Structural transformations in the crystalline sample

In Fig. 5 we show the atomic configurations of a (100) silicon slab during various stages of nanoindentation. It is clearly seen that the blunt diamond indenter moves with a negligible adhesion of the silicon atoms to the indenter surface. As a result, during unloading, the Si atoms around the indenter experience only a weak attraction to the indenter. This circumstance allows us to correctly reproduce a trend in

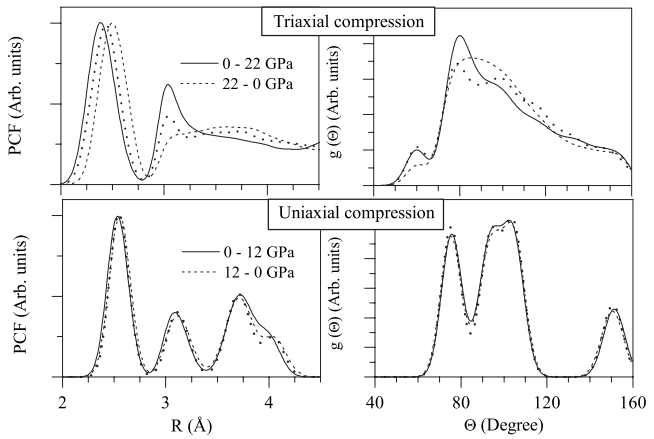

FIG. 4. Pair-correlation function (PCF, left panel) and bond-angle distribution [$g(\theta)$, right panel] for the compressed (solid line) and decompressed (dashed line) *cd*-Si structures. The dotted line in the upper and lower panels denotes the characteristics for the 512-atom HDA and β-Si phases, respectively.

the load-displacement curves that is often observed in experiments. Such curves obtained for various rates of loading and unloading are shown in Fig. 6. We note that the unloading part is mostly located above the abscissa axis, which is a consequence of the modification of the Tersoff potential. In practice, the cohesion inside an indenter or a Si slab is supposed to be higher than the adhesion of the silicon atoms to the indenter surface because of defects, contamination,

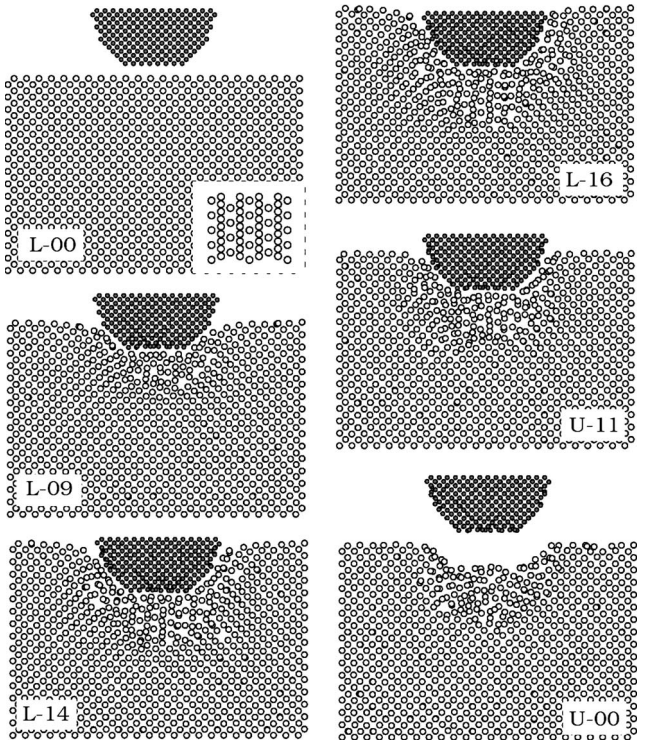

FIG. 5. Cross section of the atomic configurations of a (100) silicon slab at different stages of indentation. The numbers denote the indenter displacements, h, in Å during loading (L) and unloading (U). Open and full circles are silicon and carbon atoms, respectively. The inset shows the atomic structure of β-Si.

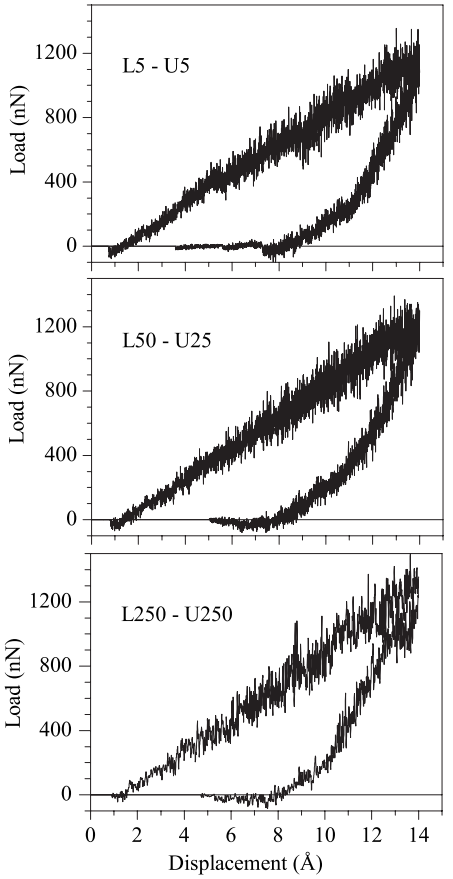

FIG. 6. Load-displacement curves of a *cd*-Si (100) slab obtained for various indentation rates. The numbers denote the rates of loading (L) and unloading (U) in m/s.

roughness, etc. Therefore, the artificial reduction in the attraction between the Si and C atoms in the Tersoff potential indirectly accounts for this circumstance. It is worth noting that in previous studies,[27–30] sufficiently strong Si-C attraction in the potential function led to an unloading curve mostly located below the abscissa axis, and unloading at high rates had to be considered to obtain a realistic picture of nanoindentation. We believe that because the tested samples are limited to a relatively small and finite number of atoms, a potential with a strong Si-C attraction leads to an unrealistic picture of indentation-induced ST, especially during unloading.

Back to Fig. 5, the evolution of a (100) silicon slab during indentation is clearly seen: in the region beneath the indenter (RBI), the distorted β-Si phase appears under certain conditions of indentation. This suggests that the onset of formation of this phase is responsible for the weak dip around $h=9$ Å in the loading curve shown in Fig. 6. This feature becomes especially apparent in the load-displacement curve obtained at low indentation rate.

As can be seen in Fig. 6, an increase in nanoindentation rate weakly changes the trend of the load-displacement curves. Nevertheless, we note a small increase in the maximum load from approximately 1200 to 1400 nN when indentation rate rises from 5 to 250 m/s. Such a behavior of the Si slab under indentation can be attributed to a weak lattice

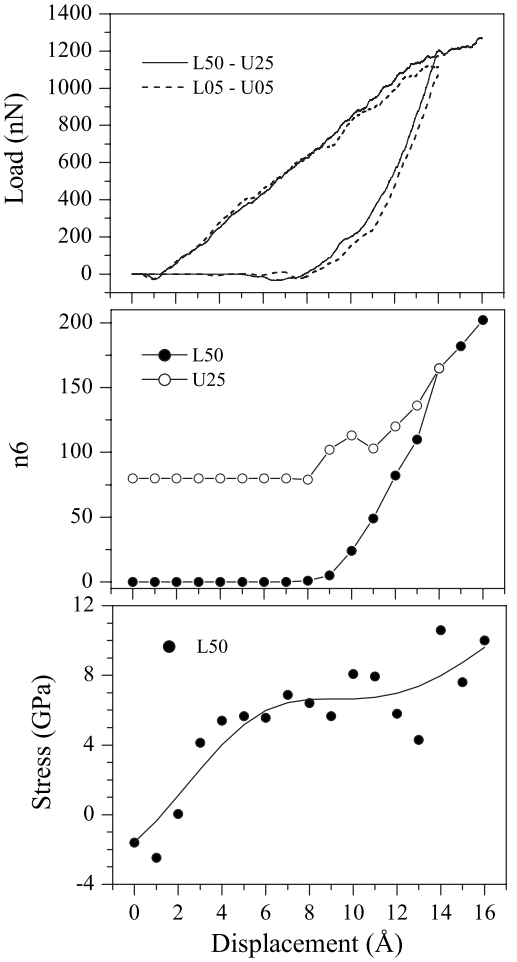

FIG. 7. Load-displacement curves, number of sixfold coordinated atoms, n6, and average intrinsic stress σ_{zz} of the atomic aggregate in the region beneath the indenter for a *cd*-Si (100) slab as functions of indenter displacement. The notation is the same as in Fig. 6. Here and later on, the load-displacement curves are averaged over 100 points, and the $\sigma_{zz}(h)$ curves are approximated with a polynomial fit. The onset of unloading corresponds to an indenter displacement $h=14$ Å.

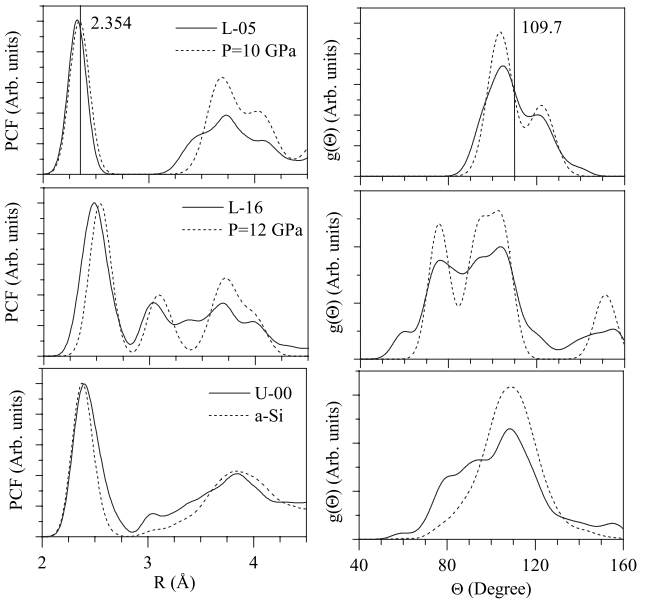

FIG. 8. Pair-correlation function (PCF, left panel) and bond-angle distribution [right panel, $g(\theta)$] of the RBI for a (100) slab during loading ($L;h=5,16$ Å) and after complete unloading ($U;h=0.0$) (solid line), and for the 4096-atom *cd*-Si sample under uniaxial compression at $P=5$ GPa and 12 GPa (dashed line). The vertical lines denote the peak positions in *cd*-Si. The respective characteristics for a 512-atom *a*-Si sample are also shown (bottom dashed curves).

relaxation at high indentation rate: the stress of the atoms in the RBI is accumulated during loading in both the transformed and untransformed regions.

In Fig. 7, the load-displacement curves, number of sixfold coordinated atoms n6, and average stress σ_{zz} of the RBI for a (100) slab are presented as functions of indenter displacement, h. The PCF and bond-angle distributions $[g(\theta)]$ associated with the atoms beneath the indenter in this slab are shown in Fig. 8. These characteristics are compared to the respective data obtained for a uniaxial compression. During the initial stage of nanoindentation, the fourfold coordination is preserved. The *cd*-Si lattice is compressed, and this is reflected in the shift of the nearest-neighbor PCF peak toward shorter distances and in the appearance of the minor peak in the bond-angle distribution. The intrinsic stress σ_{zz} reaches a plateau when the system still preserves the fourfold coordination. An increase in coordination number corresponds to the appearance of sixfold coordinated β-Si with reduced volume. The onset of formation of this phase can give rise to a pop-in in the loading curve. The atomic configuration, and the pair-correlation and $g(\theta)$ functions for the L-16 configuration presented in Figs. 5 and 8 clearly indicate the formation of a distorted β-Si phase. We note that the transformation to the β-Si phase does not occur by analogy with the pressure-induced transitions considered above, but instead is favored by a uniaxial strain, caused by the diamond indenter, by analogy with the uniaxial compression (cf. Fig. 8). In Fig. 7 the plateaulike region in the stress-displacement curve corresponds to the transformation of the RBI to β-Si that occurs at approximately 8 GPa, which is lower than the hydrostatic transition pressure of 11–12 GPa for the *cd*-Si to β-Si transition established above (cf. Table I and Fig. 2). This result confirms previous expectations according to which, under specific conditions such as nanoindentation, the transformation pressure could decrease to as low as 8 Gpa.[20] Finally, we find that for the L-13 configuration, the lattice parameters of the β-Si phase that forms in the RBI are $a=4.66$ Å and $c=2.51$ Å, and these parameters change during nanoindentation.

During unloading, the low-density *a*-Si phase is supposed to appear, and an increase in volume gives rise to the pop-out (the bend at approximately $h=10$ Å) in the unloading curve (cf. Figs. 6 and 7). The number of sixfold coordinated atoms decreases noticeably during unloading when h decreases from 14 to 10 Å but does not reach zero after complete unloading. These findings and the structural characteristics shown in Fig. 8 prompt us to conclude that the indent structure after unloading is made of a mixture of *a*-Si and disordered β-Si phases, which is consistent with experimental

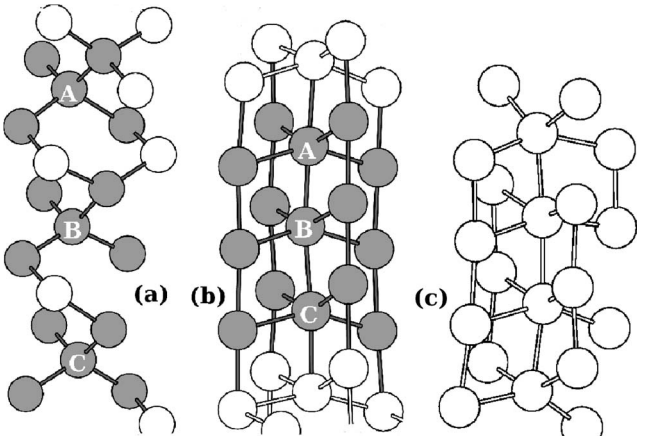

FIG. 9. Change in the tetrahedral configuration during uniaxial compression of the bulk *cd*-Si before $P=10$ GPa (a) and after $P=12$ GPa (b) the *cd*-Si to β-Si transition. The letters A, B, C denote the tetrahedron centers. For the sake of comparison, the atomic aggregate in the RBI for the L-16 configuration is also shown (c).

findings.[43–45] A structural analysis of the indent during different stages of unloading shows that the *a*-Si phase forms in the boundary layers of the RBI. Trace of the β-Si phase in the indent region upon unloading can likely be attributed to the irreversibility of the *cd*-Si-to-β-Si transition, as in the case of uniaxial decompression (cf. Fig. 4). It should be noted that the appearance of an amorphous phase does not contradict the phase diagram shown in Fig. 2.

The similarity of the changes in the structural characteristics of *cd*-Si under uniaxial strain and nanoindentation speaks in favor of the similarity that exists in the mechanisms that cause these structural changes. To understand these mechanisms, the crystalline structures immediately before and after the *cd*-Si-to-β-Si ST under uniaxial strain were analyzed. The atomic configurations of these structures are shown in Fig. 9. One can see that during uniaxial compression, the transformation from the cubic to the tetragonal structure is caused by a flattening of the tetrahedral and to a reduction of the distance between them. In the case of nanoindentation, similar changes in the atomic configurations are observed [cf. Fig. 9(c)].

To conclude this section, it should be noted that we thoroughly investigated the atomic configuration inside the RBI during different stages of nanoindentation. Despite our efforts, no dislocations under the acting tip could be found, and this seems to confirm a previous conclusion for GaAs by Chrobak *et al.*[34]

B. Structural transformations in the amorphous sample

The load-displacement response, the sixfold coordination $n6$ and the average intrinsic stress of the RBI for the *a*-Si slab as functions of indenter displacement are shown in Fig. 10. The density profile along the z direction, and the structural characteristics of the RBI for the *a*-Si slab are presented in Fig. 11 and Fig. 12, respectively. For the sake of comparison, in Fig. 12 we show the pair-correlation and $g(\theta)$ functions for *a*-Si under compression and decompression. It is

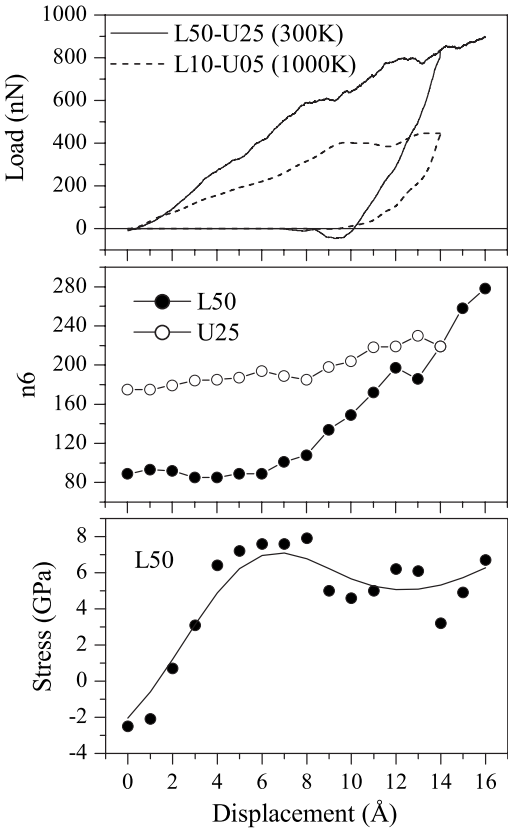

FIG. 10. Load-displacement curves, number of sixfold coordinated atoms (n6), and average intrinsic stress (σ_{zz}) of the atomic aggregate in the RBI for the *a*-Si slab as functions of indenter displacement, h. The onset of unloading corresponds to $h=14$ Å. The results of nanoindentation at 1000 K are also shown. The labels have been defined in Fig. 6.

seen that load drops take place around $h\sim 9$ Å and 13 Å. These drops correlate with periodic fluctuations of the sample density along the z direction (cf. Fig. 11). The fluctuation amplitude decreases towards the slab center. The period of the oscillations is approximately 3.57 Å, which is slightly lower than the second nearest-neighbor distance of 3.84 Å in *cd*-Si. Similar oscillations were observed for *a*-SiC.[32] The density fluctuation is attributed to a perturbation among the surface atoms and also reflects the attempt to preserve short-range order in the amorphous sample.[32] The density fluctuations influence also the stress state of the at-

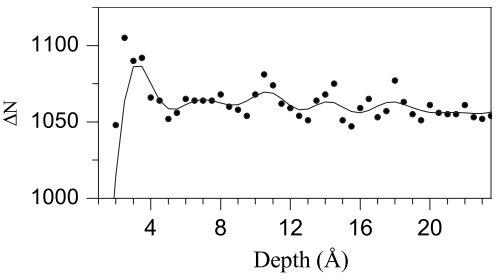

FIG. 11. Number of atoms (ΔN) in a 5 Å horizontal slice as a function of the depth of the *a*-Si slab. The solid line is deduced from an average over three points.

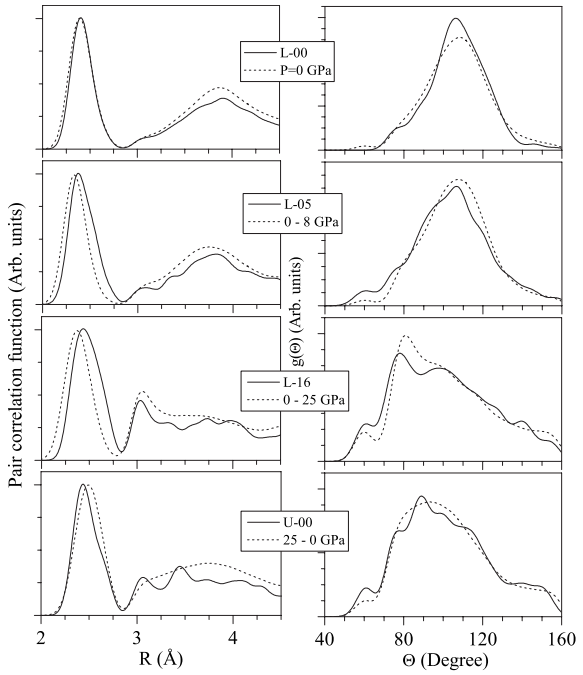

FIG. 12. Pair-correlation function (PCF, left panel) and bond angle distribution [right panel, $g(\theta)$] for the RBI of the a-Si slab at loading ($L;h=0,5,16$ Å) and complete unloading ($U;h=0.0$) (solid line), and for the 4096-atom a-Si substrate under triaxial compression (at $P=8$ GPa and 25 GPa) and complete decompression (pressure drops from 25 GPa to 0) (dashed line).

oms in the RBI, as indicated by the oscillatory behavior of the $\sigma_{zz}(h)$ curve in Fig. 10 (bottom).

While the periodic fluctuations can contribute to the load drop around $h\sim 13$ Å, we assign the drop around $h\sim 9$ Å to the a-Si→HDA transition that is accompanied by a volume reduction of the RBI and by an increase in the sixfold coordination (cf. Fig. 10). The value of $\sigma_{zz}=8$ GPa is close to the transition pressure $P_0=8.4$ GPa of the a-Si→HDA transition that is observed under hydrostatic pressure (cf. Table II). An important argument in favor of this transition is the similarity of the structural changes that occur in a-Si during nanoindentation and compression. Thus, we see that the nanoindentation of a-Si gives rise to structural changes that are similar to those caused by triaxial compression. Unlike in cd-Si, the ST in the RBI of an amorphous sample during nanoindentation will occur by analogy with uniform compression. Figure 3 shows that the structural changes during uniaxial compression are gradual, and significant changes occur at high pressures. Therefore, we predict that the atomic aggregate located beneath the indenter will undergo a mostly uniform compression because of the specificity of the amorphous structure. In the case of cd-Si, uniaxial compression leads to a flattening of the tetrahedra in the same direction. For a-Si, this does not occur since the distorted tetrahedra are randomly oriented. Therefore, the a-Si phase will be compressed homogeneously during nanoindentation.

The analysis of the structural changes of the a-Si sample during unloading (Fig. 12) shows that the distinct HDA to a-Si ST does not occur. This is also confirmed by the small variation of the sixfold coordination with displacement during unloading, see Fig. 10. These facts indicate that the path is not completely reversible upon unloading, and the final amorphous indent structure is represented mainly by the HDA phase, as in the case of the decompression of the bulk HDA phase. As a result, in the unloading curve shown in Fig. 10, we do not observe a distinct feature related to structural transformations. However, the path can be reversible provided unloading occurs at high temperature, in which case the pop-out can be shown. In Fig. 10 we present the results of nanoindentation at 1000 K, where the barely visible pop-out around $h=13$ Å is observed. The structural analysis of the indent after complete unloading (not shown) indicates the existence of a low-density amorphous phase. From these findings it follows that our results for a-Si compare favorably to the experimental data of Clarke *et al.*,[21] although under our simulation conditions, the path is irreversible (contrary to experiment), and it is only at high temperature that reversibility can be achieved.

C. Indentation-induced semiconductor-to-metal transitions

As mentioned above, the cd-Si to metallic β-Si transformation takes place during nanoindentation.[3] Experimentally, the metallic nature of the β-Si phase is inferred by a drop in the resistivity by few orders of magnitude during loading. During unloading, the amorphous semiconductor phase is observed.[17] However, other studies[43,45] have shown that, in the indented region, the metallic β-Si phase coexists with the semiconducting amorphous structure.

To shed light on the origin of indentation-induced changes in the conductivity of cd-Si and a-Si, we carried out calculations of the density of states and of the electronic localization for bulk cd-Si, β-Si, and a-Si, as well as for these materials under uniaxial and triaxial compression and decompression. In Fig. 13, we show the electronic spectra of the aforementioned structures calculated with a $sp^3s^\star$ tight-binding method discussed at the end of Sec. II. Note that bulk samples, instead of transformed RBI caused by nanoindentation, were considered for these calculations. The point is that abnormal coordinations are introduced when periodic boundary conditions are applied to a specific RBI. In addition, we expect that the main results established for the bulk samples will be similar to those for a RBI during nanoindentation because of the similarities discussed earlier in ST caused by bulk compression and nanoindentation. Figure 13 shows that bulk cd-Si is a semiconductor with a band gap $E_g\sim 1.1$ eV. The amorphous sample has strongly localized band gap states in the energy range of $-0.6-+1.0$ eV. This phase is a semiconductor with a mobility gap $E_\mu\sim 1.6$ eV, since the localized gap states practically do not contribute to conductivity. Hence, the Si structures will exhibit semiconductor-type conductivity because of the existence of a distinct band gap (cd-Si) or strongly localized states over the entire band gap region (a-Si). It is well known that in a-Si, gap states arise due to abnormally coordinated atoms or strongly distorted fourfold configurations.[40] Uniaxial compression of cd-Si leads to a widening of the valence and conduction bands. As a result, the cd-Si phase just before ST ($P=10$ GPa) is a semiconductor with a narrow band gap.

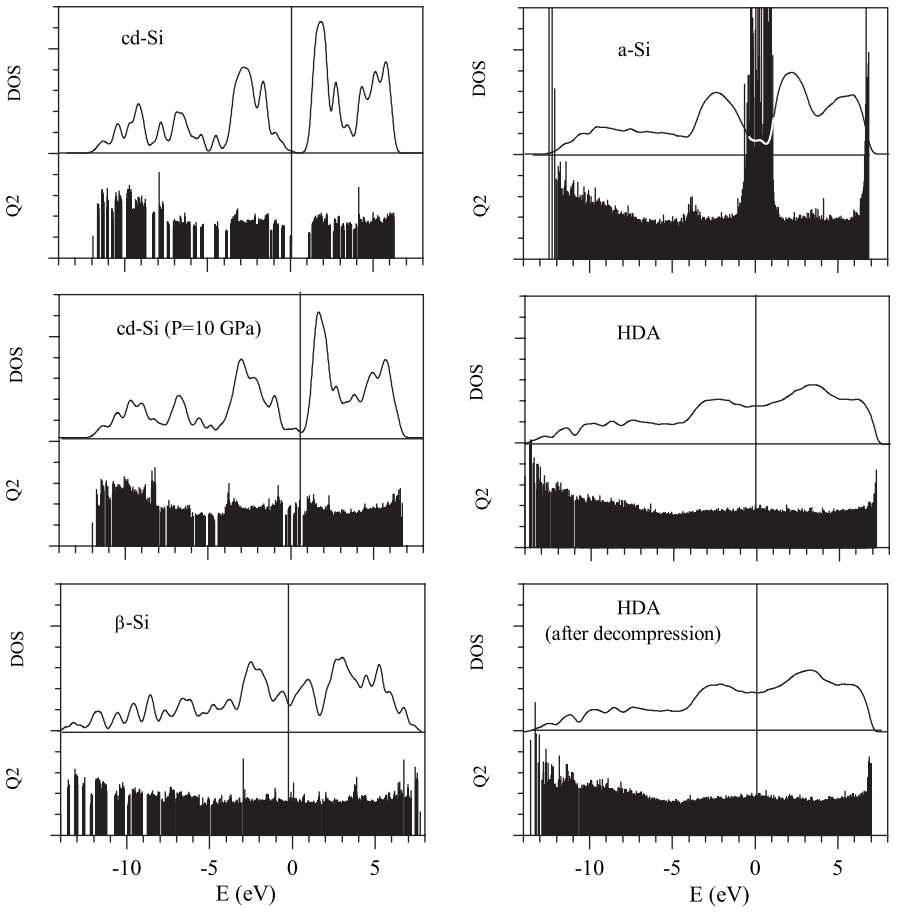

FIG. 13. Tight-binding density of states (DOS) and distribution of eigenvalues as vertical bars, where bar height is a measure of the spatial electronic localization $Q2(E)$ for *cd*-Si, *cd*-Si uniaxially compressed at 10 GPa, β-Si, *a*-Si, HDA, and decompressed HDA. Both DOS and $Q2$ are in arbitrary units. The vertical lines denote the Fermi level (the Fermi level of *a*-Si is located at 0.2 eV).

The phase after ST ($P=12$ GPa) is β-Si, and its electronic spectrum consists of extended states that give rise to metallic conductivity. During triaxial compression of *a*-Si, a change in conductivity from semiconducting to metallic occurs at $P=8-10$ GPa [25,26,40] and is due to the formation of a HDA phase. As in the case of β-Si, the extended states are responsible for the metallic conductivity of the HDA phase (cf. Fig. 13). Both the compressed crystalline and amorphous structures after low-temperature decompression do not practically change, correspondingly, their conductivity remains metallic (the spectrum of uncompressed β-Si is not shown in Fig. 13).

Given these results, let us account for the transformation of the electronic properties of the RBI during nanoindentation. By analogy with uniaxial compression, the appearance of a distorted β-Si phase in the RBI during nanoindentation implies the appearance of metallic conductivity for the indent. Upon unloading, the metallic character of the conductivity is preserved since the indent, after complete unloading, consists of a mixture of β-Si and *a*-Si, although the latter phase tends to promote a decrease in conductivity. Hence, the indent exhibits a weak metallic conductivity, which is more consistent with experimental findings[43–45] than with those reported in Ref. 17.

Coming back to the amorphous samples, we note that by analogy with triaxial compression, the formation of a HDA phase in the RBI during nanoindentation involves a change in conductivity from semiconducting to metallic (cf. Fig. 13). Upon complete unloading, the conductivity of the indent remains metallic because of the existence of this HDA phase in the indent region. Note that these transport properties can be attributed to the irreversible character of the path during low-temperature nanoindentation (cf. Fig. 12). Thus, our investigation predicts a metallic character for the conductivity of the RBI at maximum loading and upon complete unloading. Unfortunately we did not find any experimental evidence that would validate this conclusion.

V. CONCLUSIONS

Molecular dynamics simulations based on the modified Tersoff potential were carried out to study pressure-induced and indentation-induced phase transitions in crystalline and amorphous silicon. The Gibbs free energy calculations based on the Tersoff potential reveal a series of first-order phase transitions in silicon as a function of pressure: *cd*-Si$\rightarrow\beta$-Si (11.4 GPa); *cd*-Si$\rightarrow$HDA (22.5 GPa); *a*-Si$\rightarrow\beta$-Si (2.5 GPa); *a*-Si$\rightarrow$HDA (8.4 GPa).

Simulations of nanoindentation were performed for a diamond hemispherical blunt indenter. The indentation-induced phase transformations were studied as functions of hydrostatic pressure up to 11 GPa, a pressure that was reached at the contact sample-indenter during simulations. An application of the $sp^3s^\star$ TB scheme enabled us to clarify the possible origin of the semiconductor-to-metal transitions during nanoindentation.

Our findings on phase transformations and transport properties for silicon during nanoindentation are summarized as follows:

(1) For a (100) slab, the following sequence of transformations is predicted: *cd*-Si→β-Si (during loading, the pop-in is related to the appearance of β-Si) and β-Si →*a*-Si+distorted β-Si (during unloading, the pop-out is caused by the formation of *a*-Si). The observed transformations occurring during loading are explained by analogy with those caused by uniaxial compression.

(2) For the *a*-Si slab, the *a*-Si→HDA transformation is revealed (during loading, the first load drop is mainly due to the onset of this transformation, and other features are caused by density oscillations of the sample along the *z* direction). The HDA→*a*-Si transition does not occur during low-temperature unloading. However, during high-temperature unloading, this transformation should exist and be accompanied by a noticeable pop-out. These phase transformations are similar to those that take place in *a*-Si under triaxial compression.

(3) The calculations of the electronic spectra and localization for bulk *cd*-Si under uniaxial compression and bulk *a*-Si under triaxial compression enabled us to predict that during nanoindentation, conductivity evolves as follows. During loading: *cd*-Si (semiconductor, E_g=1.1 eV) → distorted β-Si (metallic conductivity). During unloading: distorted β-Si (metallic conductivity) → mixture of β-Si and *a*-Si (mostly semimetal). For the amorphous sample we predict a change of conductivity of the RBI from semiconducting to metallic during nanoindentation that is caused by the formation of a HDA phase. The metallic conductivity is preserved upon complete unloading, since this phase is still predominant in the indent.

(4) The results presented in this paper confirm the availability of theoretical models for studying structural transformations in crystalline silicon under pressure and during nanoindentation, and for providing detailed insight in new mechanisms of phase transitions in amorphous materials. Our conclusions are in rather good agreement with available experimental results.

Finally, it was shown that the Tersoff potential is able to account for almost all of the possible low-pressure modifications of silicon and most of the experimental findings on structural transformations in silicon during nanoindentation. One exception to this positive note is the failure to reproduce the *cd*-Si to β-Si transition under pressure.

ACKNOWLEDGMENTS

This work was supported in part by the Civilian Research and Development Foundation under Contract No. UK-E2-2589-KV-04. The work of P.T. was performed under the auspices of the U. S. Department of Energy by Lawrence Livermore National Laboratory under Contract No. DE-AC52-07NA27344.

[1] W. C. Oliver and G. M. Pharr, J. Mater. Res. **7**, 1564 (1992).
[2] P. Jedrzejowski, J. E. Klember-Sapieha, and L. Martinu, Thin Solid Films **426**, 150 (2003).
[3] *High-Pressure Surface Science and Engineering*, edited by Y. Gogotsi and V. Domnich (Institute of Physics, Bristol, 2004).
[4] J. C. Jamieson, Science **139**, 762 (1963).
[5] J. Z. Hu and I. L. Spain, Solid State Commun. **51**, 263 (1984).
[6] M. I. McMahon and R. J. Nelmes, Phys. Rev. B **47**, 8337 (1993).
[7] M. I. McMahon, R. J. Nelmes, N. G. Wright, and D. R. Allan, Phys. Rev. B **50**, 739 (1994).
[8] H. Olijnyk, S. K. Sikka, and W. B. Holzapfel, Phys. Lett. **103A**, 137 (1984).
[9] Y.-X. Zhao, F. Buehler, F. R. Sites, and I. L. Spain, Solid State Commun. **59**, 679 (1986).
[10] M. Imai, K. Yaoita, Y. Katayama, J.-Q. Chen, and K. Tsuji, J. Non-Cryst. Solids **150**, 49 (1992).
[11] R. H. Wentorf and J. S. Kasper, Science **139**, 338 (1963).
[12] J. Crain, G. J. Ackland, J. R. Maclean, R. O. Piltz, P. D. Hatton, and G. S. Pawley, Phys. Rev. B **50**, 13043 (1994).
[13] O. Shimomura, S. Minomura, N. Sakai, K. Asaumi, K. Tamura, J. Fukushima, and H. Endo, Philos. Mag. **29**, 547 (1974).
[14] E. R. Weppelmann, J. S. Field, and M. V. Swain, J. Mater. Res. **8**, 830 (1993).
[15] E. R. Weppelmann, J. S. Field, and M. V. Swain, J. Mater. Sci. **30**, 2455 (1995).
[16] J. S. Williams, Y. Chen, J. Wong-Leung, A. Kerr, and M. V. Swain, J. Mater. Res. **14**, 2338 (1999).
[17] D. L. Callahan and C. M. Jonathan, J. Mater. Res. **7**, 1614 (1992).
[18] I. Zarudi and L. C. Zhang, Tribol. Int. **32**, 701 (1999).
[19] L. C. Zhang and I. Zarudi, Int. J. Mech. Sci. **43**, 1985 (2001).
[20] M. C. Gupta and A. L. Ruoff, J. Appl. Phys. **51**, 1072 (1980).
[21] D. R. Clarke, M. C. Kroll, P. D. Kirchner, R. F. Cook, and B. J. Hockey, Phys. Rev. Lett. **60**, 2156 (1988).
[22] B. Haberl, J. E. Bradby, S. Ruffell, and J. S. Williams, J. Appl. Phys. **100**, 013520 (2006).
[23] F. Zandiehnadem and W. Y. Ching, Phys. Rev. B **41**, 12162 (1990).
[24] M. Bernasconi, G. L. Chiarotti, P. Focher, S. Scandolo, E. Tosatti, and M. Parrinello, J. Phys. Chem. Solids **56**, 501 (1995).
[25] M. Durandurdu and D. A. Drabold, Phys. Rev. B **64**, 014101 (2001).
[26] M. Durandurdu and D. A. Drabold, Phys. Rev. B **67**, 212101 (2003).
[27] L. C. Zhang and H. Tanaka, JSME Int. J., Ser. A **42**, 546 (1999).
[28] W. C. D. Cheong and L. C. Zhang, Nanotechnology **11**, 173 (2000).
[29] W. C. D. Cheong and L. C. Zhang, J. Mater. Sci. Lett. **19**, 439 (2000).
[30] W. C. D. Cheong and L. C. Zhang, Key Eng. Mater. **233-236**, 603 (2003).
[31] I. Szlufarska, R. K. Kalia, A. Nakano, and P. Vashishta, Phys. Rev. B **71**, 174113 (2005).
[32] I. Szlufarska, R. K. Kalia, A. Nakano, and P. Vashishta, Appl. Phys. Lett. **86**, 021915 (2005).
[33] I. Szlufarska, A. Nakano, and P. Vashishta, Science **309**, 911 (2005).

[34] D. Chrobak, K. Nordlund, and R. Nowak, Phys. Rev. Lett. **98**, 045502 (2007).
[35] J. Tersoff, Phys. Rev. B **49**, 16349 (1994).
[36] P. Blaha, K. Schwartz, P. Sorantin, and S. Tricky, Comput. Phys. Commun. **59**, 399 (1990).
[37] J. P. Perdew, K. Burke, and M. Ernzerhof, Phys. Rev. Lett. **77**, 3865 (1996).
[38] J. P. Perdew and A. Zunger, Phys. Rev. B **23**, 5048 (1981).
[39] F. Zandiehnadem and W. Y. Ching, Phys. Rev. B **41**, 12162 (1990).
[40] V. I. Ivashchenko, P. E. A. Turchi, V. I. Shevchenko, L. A. Ivashchenko, and O. A. Shramko, Phys. Rev. B **71**, 165209 (2005).
[41] J. Robertson, Philos. Mag. B **66**, 615 (1992).
[42] V. I. Ivashchenko, P. E. A. Turchi, V. I. Shevchenko, L. A. Ivashchenko, and G. V. Rusakov, Phys. Rev. B **66**, 195201 (2002).
[43] G. M. Pharr, W. C. Oliver, and D. R. Clarce, Scr. Metall. **23**, 1949 (1989).
[44] V. Domnich, Y. Gogotsi, and S. Dub, Appl. Phys. Lett. **76**, 2214 (2000).
[45] G. M. Pharr, W. C. Oliver, and D. R. Clarce, J. Electron. Mater. **19**, 881 (1990).